Check for updates

JGR Space Physics

RESEARCH ARTICLE
10.1029/2020JA028802

Key Points:

- Temporal variations of airglow emission layers, rather than fixed emission heights, are considered for more accurate wind comparison
- FPI winds are consistently smaller than MR winds and the larger discrepancies occur for OI emission layer at higher altitude
- The FPI can provide reliable height-averaged winds even under a strong wind shear near the mesopause region

Correspondence to:
C. Lee,
cslee@kopri.re.kr

Citation:
Lee, C., Jee, G., Kam, H., Wu, Q., Ham, Y.-B., Kim, Y. H., & Kim, J.-H. (2021). A comparison of Fabry–Perot interferometer and meteor radar wind measurements near the polar mesopause region. *Journal of Geophysical Research: Space Physics*, *126*, e2020JA028802. https://doi.org/10.1029/2020JA028802

Received 12 OCT 2020
Accepted 19 MAR 2021

© 2021. The Authors.
This is an open access article under the terms of the Creative Commons Attribution-NonCommercial License, which permits use, distribution and reproduction in any medium, provided the original work is properly cited and is not used for commercial purposes.

A Comparison of Fabry–Perot Interferometer and Meteor Radar Wind Measurements Near the Polar Mesopause Region

Changsup Lee[1], Geonhwa Jee[1,2], Hosik Kam[3], Qian Wu[4], Young-Bae Ham[1,2], Yong Ha Kim[5], and Jeong-Han Kim[1]

[1]Korea Polar Research Institute, Incheon, South Korea, [2]University of Science and Technology, Daejeon, South Korea, [3]Korea Astronomy and Space Science Institute, Daejeon, South Korea, [4]Chungnam National University, Daejeon, South Korea, [5]High Altitude Observatory, NCAR, Boulder, USA

Abstract The neutral winds in the Mesosphere and Lower Thermosphere (MLT) region have been observed at King Sejong Station, Antarctica using a meteor radar (MR) and a Fabry–Perot interferometer (FPI) simultaneously. These two independent MLT wind measurements are compared to each other to identify the characteristics of FPI measurement. Instead of using a fixed emission height for FPI winds, for the first time, we consider the temporal variations of airglow emission layer in association with corresponding meteor height distributions for more accurate comparison between the FPI and MR winds. The temporal variations of the airglow emission layers are examined from the inverse relationship between the height integrated emission rate and the peak emission height derived from the TIMED/SABER observations. It is found that FPI winds are consistently smaller than MR winds and the discrepancy becomes larger for OI emission at higher altitude, which may be related to large wind shear in the MLT region and variabilities of the emission layers. Finally, we found that the FPI can provide reliable height-averaged winds in the MLT region where existing a strong wind shear from this simultaneous MR wind measurements.

Plain Language Summary Simultaneous but independent observations of the MLT winds from the Fabry–Perot interferometer (FPI) and meteor radar (MR) are compared to each other to study on the characteristics of the wind measurements in the MLT region. For the first time, we used height distributions of meteor echoes to estimate the height of the OH airglow emission layers, which enables us to perform a more accurate comparison of the two measurements compared with using a fixed emission layer height. It is found that the FPI winds are consistently smaller than the MR winds and the discrepancies become larger for OI emission layer at higher altitude. However, it is also confirmed that the FPI wind measurements in the MLT region can still provide reliable winds even under the strong wind shear in the region.

1. Introduction

The Mesosphere and Lower Thermosphere (MLT) region has been studied to understand the dynamical interactions with the lower atmosphere via atmospheric waves, including planetary waves, tides, and gravity waves originated from the lower atmosphere. As the amplitude of the waves increases exponentially with height as they propagate upward, the dynamics and thermal structures of the MLT region can be severely disturbed by the effects of atmospheric waves. Therefore, the observations of the MLT neutral winds are important to investigate the dynamical effects of the waves on the region. In particular, the neutral winds in the MLT region can provide the essential information as to the wave induced residual circulation from summer to winter pole and dynamical variabilities propagating from the lower atmosphere. Ground-based optical measurements of airglow emissions are one of the most widely used techniques for the study of the MLT region. Interferometry techniques such as Fabry–Perot interferometer (FPI) and Michelson interferometer (MI) have provided neutral winds or temperatures at the representative airglow emission layers using their Doppler information (Won et al., 2001a; 2001b; Meriwether, 2006; Wu et al., 2008) while airglow imagers have been used to extract small-scale gravity wave signatures within the field of view (Taylor et al., 1995; Espy, 2004; Matsuda et al., 2014; Kam et al., 2017). Although the optical instruments provide

several valuable upper atmospheric parameters at relatively low cost, their performance and continuity of data records are limited only to moonless clear night condition over the observation site. Furthermore, most of airglow observations from ground-based optical instruments rely on the underlying assumption of the fixed height profile of airglow emission layers (Won et al., 1999; Dunker, 2018). The height of hydroxyl (OH) emission layer is assumed to be 87 km with a full width at half maximum (FWHM) of about 8 km (Baker & Stair, 1988) and the height of OI-green line emission layer is widely known to be 97 km with a FWHM of 7 km (Yee & Abreu, 1987). However, the true heights of airglow emission layers are not fixed at all but vary not only with times of day and seasons (Gao et al., 2010; Smith et al., 2010) but also with locations (Liu et al., 2008; Wüst et al., 2019). In particular, the temporal variations of the emission peak height can have a significant impact on the characteristics of the physical parameters of the MLT region derived from the ground-based observations of the airglow layers. Sheese et al. (2014), for example, showed that the ground-based observations of temperature can be biased as much as ±4K without consideration of the temporal variations of airglow emission layers. Moreover, the neutral winds in the MLT region vary rapidly with height and the magnitudes of wind shear continuously increase to the peak at around 100–110 km altitude (Larsen, 2002). This highly variable characteristic of the MLT wind makes it difficult to precisely determine the wind from the measurements of airglow emissions and therefore the large integration time may be needed for better estimate of wind.

In addition to the optical observations of the neutral winds in the MLT region, completely independent measurements have been performed by radar techniques. For example, a meteor radar (MR) has been widely operated to monitor the neutral winds and temperature in the MLT region. While the optical measurements produce winds only at particular airglow emission layers and only for clear moonless nighttime, the MR is able to provide the vertical profiles of the winds in the altitude range of 70–110 km for all local times regardless of weather conditions. However, the MR observations require a certain amount of time (∼an hour) at a given height bin to ensure enough number of meteor echoes and the vertical resolution of the wind profiles is also significantly affected by meteor detection rate. With their own limitations of the FPI and MR wind measurements, therefore, simultaneous operations of both instruments at a single site would be beneficial not only for the cross-validation of the measurements but also for the complement of the MLT wind measurements at the site.

There are only a few studies on the comparison between the mesospheric winds from optical and radar observations Plagmann et al. (1998). determined airglow heights from the correlation analysis of MR and Fabry–Perot Spectrometer (FPS) wind measurements in South Island of New Zealand Greet et al. (2000). performed a comparison of optical and radar measurements and found a good agreement in mean wind and tidal parameters determined from FPS and MF radar measurements of winds at 86 km in Antarctica. They also pointed out that the comparison of the two wind measurements can be improved by better matching sampling intervals. Most of these previous studies assumed fixed heights of the airglow emission layers in determination of the winds and for the comparisons with the radar measurements. However Yu et al. (2016) found that the variations of peak heights of the emission layers could significantly affect the correlations between the FPI and MR winds. Their results suggest that the highly variable peak heights, rather than fixed at certain heights, may reduce the accuracy of the measurements of the wind from the FPI.

In this study, we further investigate the temporal variations of the peak heights of airglow emission layers using height distributions of meteor echoes and by comparing with the Aura/MLS and TIMED/SABER measurements of the OH volume mixing ratio and OH volume emission rate, respectively. Then the FPI wind measurements are compared with vertically weighted mean MR winds at the varying heights, rather than fixed heights, of the airglow emission layers to identify the characteristics of each measurement. In Section 2, the MLT winds observed from the FPI and MR at King Sejong Station and two satellite observations are briefly described and the results of the study are presented in the following Section 3 with relevant discussions. Finally, summary and conclusion will be presented in Section 4.

2. Observations and Data Analysis

2.1. King Sejong Fabry–Perot Interferometer (KSS-FPI)

A Fabry–Perot interferometer (FPI) has been operated at King Sejong Station (KSS), the first Korean Antarctic Research base near the end of Antarctic Peninsula (62.22°S 58.79°W) to study the climatology of upper atmospheric winds and temperatures in the southern polar region since January 2017. The KSS-FPI was developed by National Center for Atmospheric Research (NCAR) and had been operated at Palmer Station in Antarctic Peninsula until 2012 before it was transferred to KSS in 2017. It is a high-resolution spectrometer capable of detecting small wavelength shifts with a 10-cm clear aperture etalon and the integration time of 3 min are needed for collecting airglow information from a narrow sky area (~1.5°). A detailed description of the FPI operation mode and its observational geometry can be found in (Wu et al., 2004; Kwon et al., 2018).

For the comparison with MR observations in the MLT region, two emission layers from OH (7–3, 892.0 nm) and OI (557.7 nm) are used to derive the neutral winds in 2017 and 2019. The FPI data in 2018 are omitted since the MR data were not available. For the effective data selection under clear sky, a cloud identification procedure was adopted using a co-located Boltwood cloud sensor which indirectly detects cloud cover from the sky temperature derived from infrared radiation (8–14 μm) of the sky. The sky condition is determined to be cloudy if the sky temperature is lower than the ambient temperature by 35 °C, which is stricter than widely accepted difference of 25 °C (Harding et al., 2019). In 2019, however, the weather information from the cloud sensor were not available and therefore wind data for clear night were manually selected based on the all-sky imager observations for the sky condition at KSS.

2.2. King Sejong Meteor Radar (KSS-MR)

The MR developed by ATRAD Pty Ltd. has been operated to continuously monitor mesospheric winds and temperatures at King Sejong Station (KSS) in Antarctica (62.22°S, 58.79°W) in collaboration with Chungnam National University, Korea, since March 2007 (Jee et al., 2014). The KSS-MR collects underdense meteor echoes within a horizontal radius of about 200 km near the mesopause region. The number of meteor echoes detected by the KSS-MR reaches up to 40,000 per day in summer but it drops to about 15,000 in winter since the peak power was upgraded from 8 to 12 kW in January 2012. The large number of meteor echoes enables us to observe the neutral winds even beyond the typical meteor detection height of 80–100 km with a better temporal resolution and to estimate mesospheric temperatures from daily meteor height distribution. A more detailed descriptions of the KSS-MR can be found in (Lee et al., 2013). Since there was a transmission hardware failure for several months in 2018, the KSS-MR wind data were used only for 2017 and 2019 in the comparison with the KSS-FPI observations.

MR and FPI are the most widely used radar and optical instruments, respectively to observe neutral winds in the MLT region but there are inherent differences in their observational characteristics such as different field of views and temporal resolutions for estimating winds from the observations. To minimize unintended wind discrepancies caused by different observation times, we selected meteor echoes observed within a zenith angle of 20–65° to calculate mean MR winds for the 48-min time window around the FPI observation time. Both wind measurements are binned into every hour to obtain hourly mean winds at each emission layer. In the calculation of MR wind, the height averaging process within a height bin was performed by applying a Gaussian shaped weighting function with a FWHM of 12 km to reflect the vertical profiles of the airglow emission layers. This process can notably reduce the effect of the background wind shear on the FPI wind estimation. Note that the vertical width of a height bin for the MR wind estimation is larger than a typical thickness of the airglow emission layers in the MLT region to take account of the vertical variations of the airglow emission layers for more accurate comparison between the two measurements.

2.3. Satellite Observations for Airglow Emission

For more accurate comparison between the mesospheric winds obtained from ground-based optical and radar instruments, we also consider the temporal variations of airglow emissions in the MLT region using two satellite observations of TIMED/SABER and Aura/MLS: They provide vertical profiles of the OH airglow

emission intensity and the OH volume mixing ratio. Although the time periods of observations from satellites and ground-based instruments are different, it is still worth investigating the temporal variations of the airglow emissions from different types of observations.

2.3.1. TIMED/SABER

The Sounding of the Atmosphere using Broadband Emission Radiometry (SABER) instrument is one of the four instruments on board NASA's TIMED (Thermosphere Ionosphere Mesosphere Energetics Dynamics) satellite to measure the limb emissions in the ten-broadband infrared channels covering from 1.27 to 17 μm. The volume emission rate (VER) profiles are derived from the two mesospheric hydroxyl (OH) airglow emissions. The OH-A channel is centered at 1.64 μm to measure airglow emissions from OH (4–2) and OH (5–3) vibrational transitions while the OH-B channels is centered at 2.06 μm to mainly capture the emissions from OH (8–6) and OH (9–7) vibrational transitions with a height resolution of about 2 km (Baker et al., 2007). For the comparison with ground-based observations at KSS, the SABER data are restricted to those within 5° latitude bin around 62.2°S with solar zenith angle of 105°. Note that the satellite and ground observations are compared each other for different period since there is no satellite data available for the observations at KSS. We examined the year-to-year variability of the satellite observations for the MLT region for the 5-year period of 2005–2009. It was found that the interannual variations of the OH emission profiles are low enough to be compared with the KSS observations for the different periods.

2.3.2. Aura/MLS

The Microwave Limb Sounder (MLS) instrument on board the Aura satellite measures OH thermal emission from 2.5 THz rotational lines in the ground vibrational state. A single profile of the OH Volume Mixing Ratio (VMR) is obtained by a vertical limb scanning for 24.6 s extending over 18–94 km. The vertical resolutions of the observation vary with the altitude and drops to ∼15 km at 0.001 hPa from 5 km at 100 hPa (Schwartz et al., 2008). The local solar time at the latitude of KSS (62.2°S) is nearly fixed at around 00-01LT for the descending (night) modes of the orbit. The MLS OH VMR measurements are provided for the period of 2005–2009 until the local oscillator was deactivated in 2009. In this study, we used the zonal mean OH VMR data from descending node within a 5° latitude bin centered on the latitude of KSS to retrieve the pressure dependence of nighttime OH airglow emission profiles. The MLS geopotential height (GPH) was converted to geometric height for the comparison with ground-based MR measurements at KSS.

3. Results and Discussions

3.1. Temporal Variations of the OH Airglow Emission Layer

Since the neutral winds derived from the FPI measurements represent the drift motions of molecules emitting the airglow within emission layers, the state of the background atmosphere should be considered in the comparison with MR wind measurements. Considering the seasonal variations of the atmospheric structures in the MLT region, the airglow emission layer represented by a peak emission height and height integrated intensity should also experience corresponding seasonal variations (Zhang & Shepherd, 1999; Gao et al., 2010). In particular, a number of studies reported that the airglow emission layers are intimately related to constant pressure surfaces in the region. For example Pickett et al. (2006) showed from the MLS observation that a nocturnal OH density clearly follows a constant pressure surface regardless of latitude. Reid et al. (2017) also found that OH airglow emission heights follow constant density surfaces using the SABER and MR observations. Recently, it was reported that the height distributions of meteor echoes detected by the MR are well correlated with background atmospheric pressure (Lee et al., 2018a). The meteor peak height (MPH) closely follows a constant atmospheric pressure and the width of meteor height distribution (Full-width at half maximum, FWHM) remarkably reflects the vertical structure of the background atmospheric pressure. Using the relation between the airglow emission profile and meteor height distribution reflecting the background atmospheric pressure, we can estimate the temporal variations of the airglow emission layer on a daily basis from the MPH and FWHM determined from the MR observations.

Figure 1a shows the pressure levels of zonal mean nocturnal OH volume mixing ratio (VMR) at the latitude of KSS derived from the MLS during 2005–2009. The layer of peak OH VMR is mostly located on the pressure level of $\log_{10}P = -2.33$ during winter season from March to September but it moves to the lower

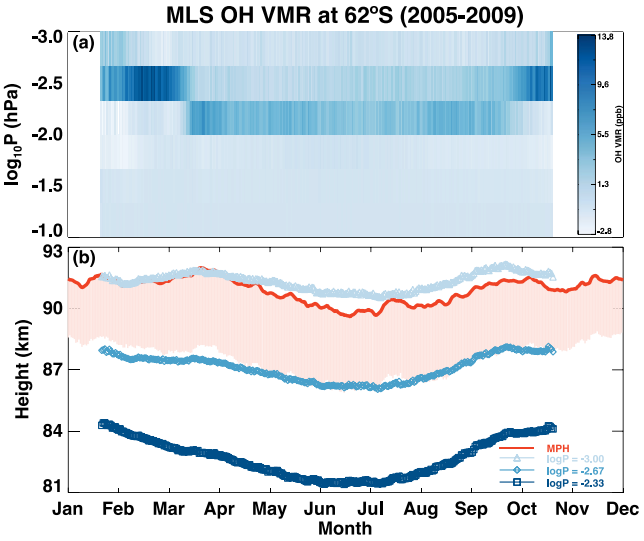

Figure 1. (a) Pressure levels of 5-year zonal mean nocturnal OH volume mixing ratio (VMR) at KSS derived from the MLS in 2005–2009 and (b) the height distributions of fixed pressure layers. The meteor peak height (MPH) (red solid line) and one third of the FWHM (light red shaded area) estimated are also presented to show the relationship with background pressure levels.

pressure level of $\log_{10}P = -2.67$ during summer season from October to February. Since the KSS-FPI measures the winds only during winter season from March to October, we assume that the peak height of the OH emission layer mostly follows a fixed pressure surface during the entire observation period. We used one-third of the FWHM in Figure 1b to show its great correlation with the background atmospheric pressure. As shown in Figure 1b, the atmospheric pressure shows a clear annual oscillation being highest in summer and lowest in winter below about 90 km altitude but it becomes semiannual oscillation with two peaks at the both equinoxes above that altitude. Note that the MPH and FWHM are well correlated with the MLS pressure surfaces in all seasons. As the MPH represents approximately a fixed atmospheric pressure surface of about $\log_{10}P = -3$, we can expect that the temporal variations of the peak OH VMR can be estimated using the MPH and FWHM.

The SABER measurements of height profiles of OH volume emission rates (VERs) centered at 1.6 and 2.0 μm are analyzed to examine the local time variations of the airglow emission layers. Figure 2a depicts the relation between OH peak emission heights and height integrated emission rates (IERs) from OH-1.6 and OH-2.0 measurements at 62°S latitude in the period of 2005–2009. As several previous studies pointed out, there is a notable inverse relationship between the emission peak height and the IER (Liu & Shepherd, 2006; Baker et al., 2007). The IER of OH-2.0 emission is mostly smaller and distributed at higher altitude than OH-1.6

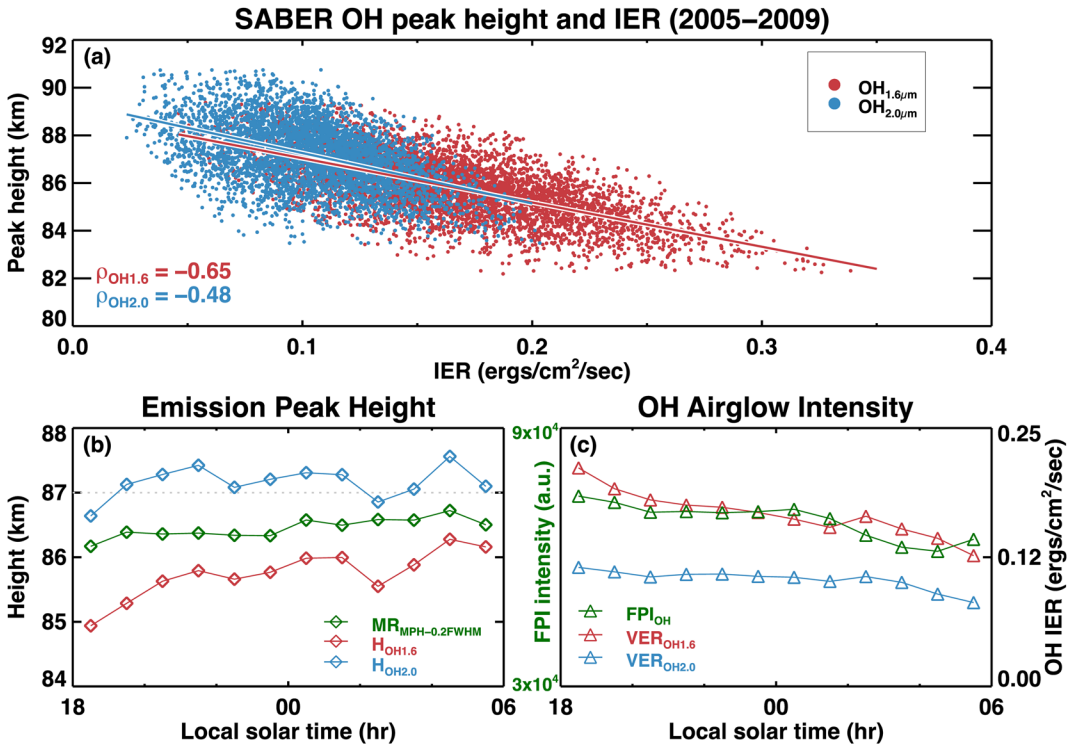

Figure 2. (a) SABER nighttime OH 1.6 μm and OH 2.0 μm emission peak heights versus height integrated emission rates (IERs) over the entire longitudes at 62°S during 2005–2009. (b) Local time variations of OH-1.6 μm and OH-2.0 μm emission peak heights. The height layer of MPH-0.2FWHM is also presented for temporal dependence of background atmospheric pressure. The gray dotted line represents the height of 87 km. (c) Local time dependence of the OH-1.6 μm and OH-2.0 μm IERs. Note that the airglow intensity (green triangle) measured by the KSS-FPI closely follows two SABER OH IERs.

emission. There are significant scatters (i.e., correlation coefficients) in Figure 2a and they are probably attributed to spatial variabilities of the airglow emission by gravity waves in the MLT region (Yee et al., 1997). Note that the scatters for OH-2.0 emission at higher peak height are larger than for OH-1.6 emission at lower peak height since the amplitude of gravity wave increases with altitude. The longitudinal variations of the OH emission properties caused by tides may further contribute to the scatter of the zonal mean emission rates (Xu et al., 2010).

Figure 2b shows the local time variations of the OH emission peak heights (red and blue lines) during nighttime. The differences between 1.6 and 2.0 μm emission peak heights are about 2 km before the midnight but decreases down to about 1 km in the morning, which is consistent with previous studies on the OH emission peak height (Savigny et al., 2012; Sheese et al., 2014) showing that the emission peak height increases with increasing vibrational level. Savigny et al. (2012) found that OH emission peak heights increase roughly by 0.5 km per vibrational level using the three different OH Meinel bands retrieved from the Envisat/SCIAMACHY. As for the local time variations, both SABER OH emission peak heights show similar local time variations except that 1.6 μm OH emission peak height tends to increase with local time. The layer of MPH-0.2FWHM representing the constant atmospheric pressure surface exists between two OH emission peak heights and it is displayed by green line in Figure 2b. Although the atmospheric pressure surface shows similar local time variations to SABER OH emission peak heights, more complicated temporal variations appear in the emission peak heights. This discrepancy may indicate that airglow emission peak heights are not solely determined by the background pressure but there may be other additional factors. Figure 2c shows the local time variations of the OH height integrated emission rates (IERs). Also depicted by green line in the figure is the airglow intensity measured by the KSS-FPI, which shows consistent local time variations with SABER OH measurements. The OH airglow emission observed by KSS-FPI is emanated from OH (7–3) vibrational transition which is an intermediate line between OH (4–2)/(5–3) for 1.6 μm and OH (8–6)/(9–7) for 2.0 μm. Therefore, the FPI OH emission layer should be located between SABER OH-1.6 μm (lower altitude) and OH-2.0 μm (higher altitude) with similar local time variations. This is confirmed by the FPI airglow emission intensity presented in Figure 2c. Ghosh (2002) also showed that both the OH emission intensities and their fluctuations from all vibrational transition lines are strongly correlated to each other.

3.2. Comparison Between FPI and MR Wind Observations

Figure 3 shows the height distributions of the correlation coefficient between FPI and MR hourly mean winds for OH and OI green line emissions in 2017 and 2019. For this comparison with FPI winds at each emission layer, MR winds are calculated at 11 different height layers relative to the MPH (H_0) with height bins which are proportional to the FWHM to consider the seasonal variations of the atmospheric pressure. The correlations between the two winds show the maximum at the height of MPH (corresponding to about 89.2–91.6 km) for OH emission and at the height of MPH+0.6FWHM (96.4–98.8 km) for OI emission. The heights of the maximum correlation are considered to be true heights of the FPI-observed airglow emission layers for OH and OI assuming that both measurements of neutral motions represent reasonable winds. Although these heights of OH and OI airglow layers determined by the correlation analysis are in good agreement with previous studies (Baker & Stair, 1988; Taylor et al., 1995), these values are slightly higher than traditionally known heights of the airglow emission layers (87 km for OH and 97 km for OI). Plagmann et al. (1998) also found that the airglow heights derived from the correlation analysis between MR and FPS winds are larger than the nominal airglow emission heights. Note that there is an obvious difference in the height profiles of correlation coefficient between OH and OI emissions. The correlation coefficients for OI much more rapidly decrease as the height moving away from the peak correlation altitude than the correlation coefficients for OH. This result indicates that the neutral winds rapidly change with height at higher altitude in the MLT region (Larsen, 2002).

For a direct comparison between the FPI and MR wind measurements, we selected height layers of the MR winds at the heights of maximum correlations with FPI winds. Figure 4 shows the scatter plots of FPI versus MR winds for zonal (left) and meridional (right) components at the OI (top) and OH (bottom) emission layers. FPI winds at OH emission layer better agree with MR winds with smaller scatters than the winds at OI emission layer, which implies that the neutral winds from OI emission layer at higher altitude shows larger

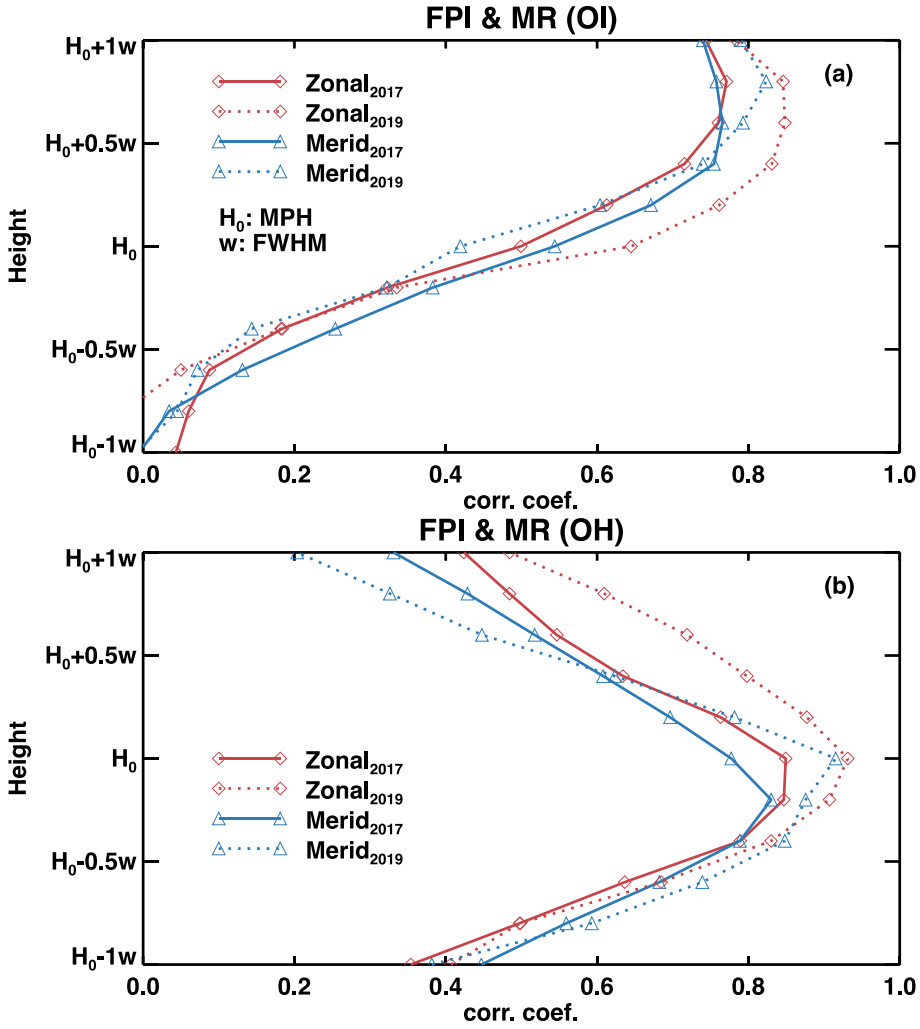

Figure 3. The vertical profile of correlation coefficients between the FPI and MR hourly mean winds for the OI-557.7 nm (a) and OH (b) airglow emissions in 2017 and 2019. The MR winds were calculated at 11 different layers determined by the MPH and the FWHM to consider seasonal variations of airglow emission layers.

variabilities. This result indicates that the neutral winds are more severely disturbed by gravity waves with larger amplitudes at higher altitudes. Compared with the correlation coefficients between the two measurements in 2017 (Lee et al., 2018b), they are greatly improved from 0.32–0.6 to 0.77–0.93 by better matching of the sampling range in both height and time between the FPI and MR. However, the correlations are still lower than the results of previous studies (Plagmann et al., 1998; Yu et al., 2016). It should be noted that our comparison is performed between simultaneous MR and FPI wind measurements at a single site but the MR and FPI observations at previous studies were not performed at a single site but separated by a few hundred kilometers. It is well known that the gravity waves propagating from the lower atmosphere contribute to severe perturbations in dynamics and composition of the upper atmosphere near the Antarctic Peninsula and the southern Andes where it is recognized to be hot spots for strong gravity wave activity (Baumgaertner & McDonald, 2007; Park et al., 2014). Phillips et al. (1994) also found from the UARS WINDII measurements that the altitude of the emission peak varies on the order of a scale height (~6 km) due to the internal gravity waves. The large variations of the emission layer heights should contribute to larger wind discrepancies between the FPI and MR at KSS. While the FPI winds are vertically integrated, the MR winds are horizontally weighted. The different weighting of each of the measurement can also contribute the discrepancy between the two data sets. Gradients in vertical and horizontal directions can impact each data quite differently.

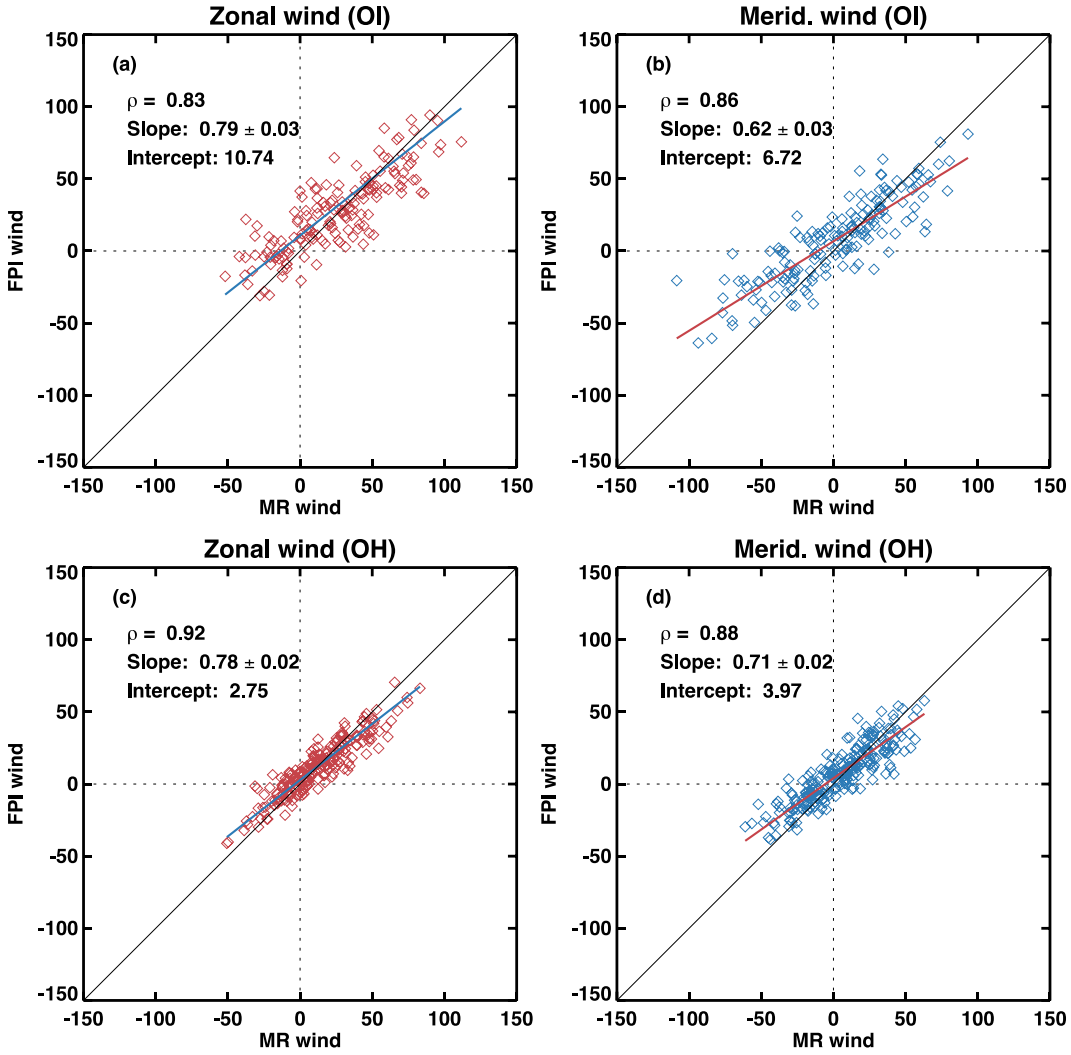

Figure 4. Scatterplots of hourly mean zonal and meridional wind components at OI layer (a), (b), OH layer (c), (d) measured by the FPI and MR in 2017 and 2019, respectively. The 2-year averaged correlation coefficients (ρ), linear slopes, and intercepts are presented on each scatterplot. The colored solid line denotes the regression line of FPI against MR winds. The black solid line shows the line of equality.

The comparison between the FPI and MR winds at two emission layers is summarized in Table 1. The observation time of FPI wind in 2019 is notably shorter than that in 2017 because the stricter condition for clear sky was applied to the FPI observations in 2019 using all-sky imager data instead of using the cloud sensor as in 2017. The correlation coefficients of the FPI-MR wind comparison are larger in 2019 than in 2017 for both OI and OH emissions and also the slopes for OH emission are closer to unity in 2019. It should be noted that slightly lower slopes for OI emission in 2019 are only a statistical result caused by relatively shorter observation time manifested by higher standard errors. The slopes less than unity obviously implies that FPI wind speeds are generally smaller than MR wind measurements. The relatively better agreement of the FPI-MR wind comparison in 2019 indicates that the FPI observation is significantly affected by sky condition and more specifically it tends to underestimate the neutral wind under the cloudy condition. In other words, the cloudy sky condition may contribute to lower Doppler shifts and in turn to reduce the resulting wind speed. This result also suggests that the identification of clear sky condition is critical to guarantee the accuracy of the FPI wind measurements.

Table 1
FPI-MR Wind Comparison for Two Airglow Emission Layers in 2017 and 2019

Emission (wavelength)	Wind component	Year	Observation hours	Correlation coefficient	Slope	Intercept (ms^{-1})
OI (557.7 nm)	Zonal	2017	97	0.77	0.80 ± 0.04	12.95
		2019	60	0.85	0.77 ± 0.06	5.14
	Meridional	2017	102	0.77	0.64 ± 0.03	4.43
		2019	62	0.82	0.59 ± 0.05	10.81
OH (892.0 nm)	Zonal	2017	132	0.85	0.74 ± 0.03	2.52
		2019	80	0.93	0.82 ± 0.04	2.96
	Meridional	2017	143	0.83	0.67 ± 0.03	3.47
		2019	87	0.92	0.79 ± 0.04	4.68

3.3. Background Atmospheric Conditions for the Wind Measurement

To further evaluate the effect of cloud cover on the FPI observations, we classified the FPI wind data in 2019 according to the sky temperature. Figure 5 shows the correlation coefficients and the slopes of FPI-MR wind comparison as a function of sky temperature for two emission layers. Both parameters notably increase as the sky temperature decreases and reach maxima at about −40∼−45 °C. The larger correlation coefficient and slope indicate better agreement between FPI and MR wind measurements. Below this sky temperature, the number of available FPI wind data becomes statistically too small to correctly define meaningful

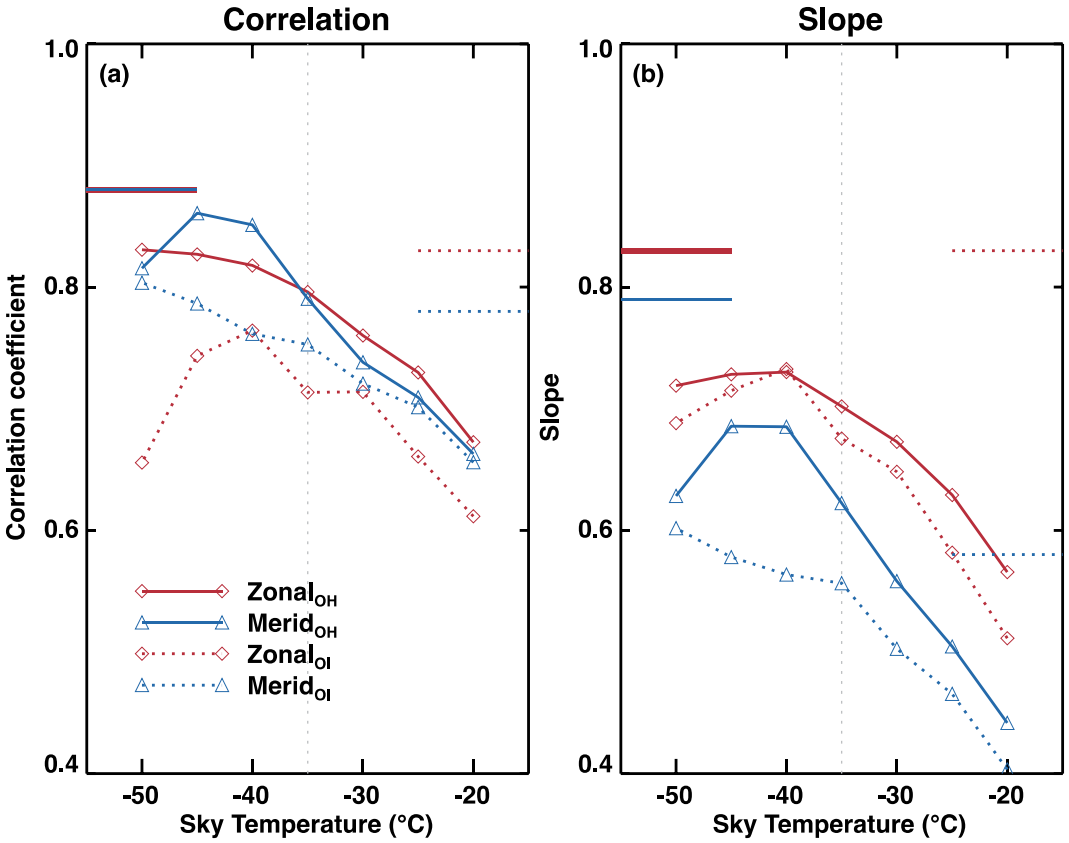

Figure 5. Correlation coefficients and slopes between FPI and MR winds as a function of sky temperature in 2019. Solid lines indicate parameters for OH emission and dotted lines for OI emission. Parameters under clear night identified from the all-sky imager also presented as solid (dotted) horizontal bars on left (right) axis for OH (OI) emission.

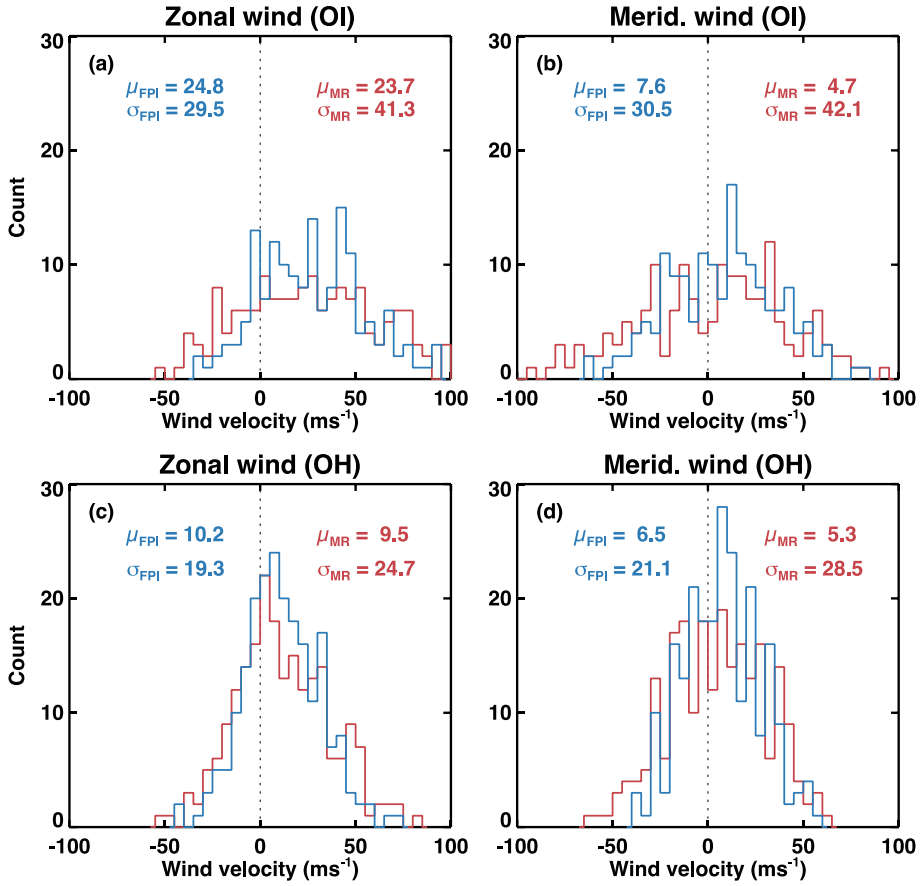

Figure 6. Histograms of FPI (blue) and MR (red) hourly-mean wind data during 2017 and 2019. Mean (μ) and standard deviation (σ) for each data are calculated from a least-squares fit using Gaussian curve.

correlation and slope with respect to MR winds as seen in their declining tendency at lower sky temperature below about −45 °C in Figure 5. Note that even the best results of two parameters from the sky temperature are still worse than those from the all-sky imager data in both airglow emissions. As the cloud sensor provides only the average information of cloudiness by measuring the IR emission from the sky with a large field of view (80–120◦), it may fail to ensure the clear sky condition for individual FPI observation points. In other words, although it is defined to be "clear" by the cloud sensor, any of 4 sampling directions of the FPI observations can be in the cloudy condition to result in inaccurate measurements of winds. It should be noted that all the slopes of the plots never reach unity, which indicates that FPI winds are consistently smaller than MR winds for both OH and OI emissions. Furthermore, the slopes are lower at the OI layer than the OH layer, which shows that the differences between FPI and MR winds become larger at higher altitude. The distributions of horizontal wind measurements from MR and FPI in 2017 and 2019 are presented in Figure 6. As already shown in Figure 4, there is a larger spread in wind distributions at OI layer compared to those at OH layer. Both measurements show typical high-latitude winds in the MLT region. In other words, zonal winds mostly flow eastward while there is no conspicuous direction in the meridional winds (Sandford et al., 2010; Fritts et al., 2012). Although the two measurements relatively well agree in terms of mean winds, there are significant differences in the standard deviation: MR winds are more widely dispersed compared to the FPI winds at both emission layers.

Note that there are remarkable differences between the wind distributions of OI and OH in Figure 6. The winds from OI emission at higher altitude are more broadly distributed to larger wind velocity than the winds from OH at lower altitude. This result indicates that both components of the winds tend to be increased with height in the region of emission layers. It is well known that the neutral winds in the MLT region steeply vary with height and the magnitude of the resulting wind shear continuously increases to

Table 2
Peak Magnitude of the Vertical Wind Gradient (dU/dz), the Median Wind Speed Ratio of MR-FPI, and their correlation coefficients at Two Emission Heights in 2017 and 2019

Emission (wavelength)	Wind component	Year	Max. $\lvert dU/dz \rvert$	Median speed ratio (U_{MR}/U_{FPI})	Correlation coefficient
OI (557.7 nm)	Zonal	2017	9.99	0.94	0.03
		2019	10.11	1.02	0.05
	Meridional	2017	11.68	1.21	0.07
		2019	11.91	0.93	−0.04
OH (892.0 nm)	Zonal	2017	9.89	0.99	−0.02
		2019	9.67	1.00	0.06
	Meridional	2017	10.13	1.17	0.01
		2019	7.33	1.01	−0.12

reach the maximum at around 100 km altitude and then decreases rapidly above the peak altitude (Larsen, 2002).

(Yu et al., 2017) pointed out that the strong wind shear around the airglow emission layers may be responsible for discrepancies between FPI and MR wind measurements. We compared the vertical gradient of the wind with the ratio of the MR and FPI winds to evaluate the effect of the background wind shear on the observed FPI and MR winds. The vertical gradients of the wind as an indicator of the wind shear were calculated by fitting the MR winds to the linear fitting model over a given height range. Table 2 presents the maximum magnitude of the vertical wind gradients and the median wind speed ratio of MR-FPI at two emission layers in 2017 and 2019. It seems to be obvious from the extremely small correlation coefficients that FPI winds from both emission layers are hardly affected by the background vertical wind structure in this wind comparison. This can be readily explained by the fact that the height averaging process of the MR winds can significantly reduce the effects of the wind shear on the FPI wind measurements. From this result, we can conclude that the FPI provides a height-averaged wind at a nominal airglow emission layer.

Figure 7 shows the local time variations of MR and FPI winds during nighttime between 20 LT and 04 LT derived from the superposed epoch analysis applied to the wind measurements for 60 days centered on the June solstice. There exists a notable 12 h tidal signature with 3 h phase difference between zonal and

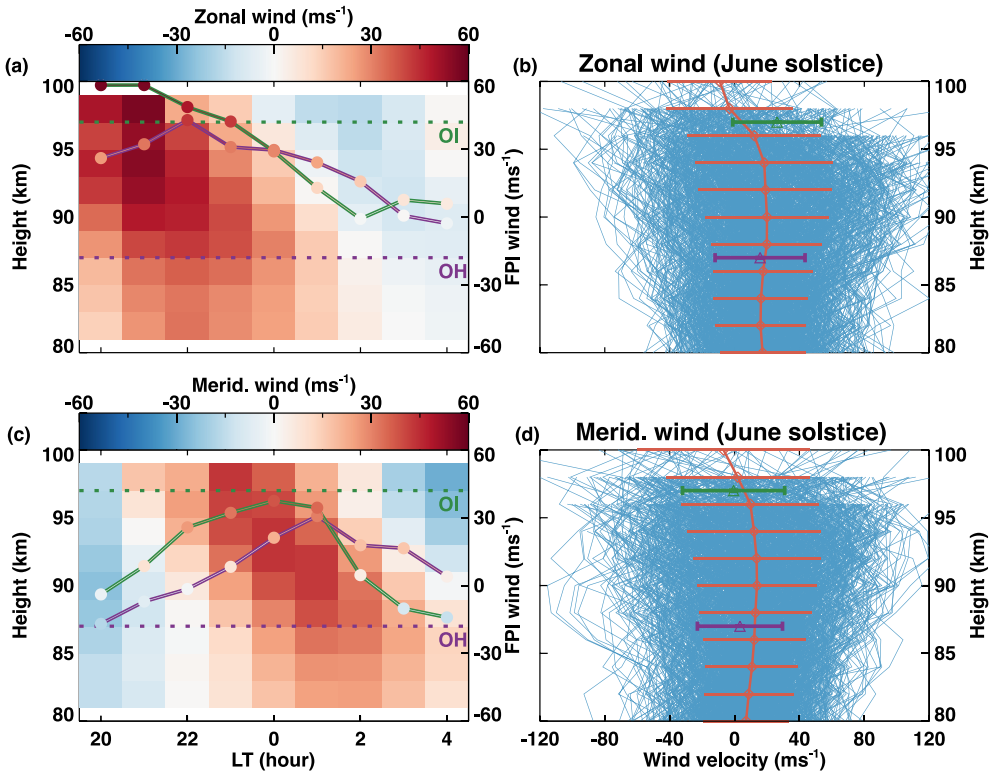

Figure 7. Local time variations of (a) zonal and (c) meridional winds from the superposed epoch analysis for 60 days centered on the June solstice in 2017/2019. FPI winds at OH and OI emission layers are also presented by color-filled circles with purple and green solid lines, respectively. Height profiles of the nighttime (b) zonal and (d) meridional hourly mean winds are displayed on the right panels during 60 days around the June solstice. The mean winds with standard deviations are presented by red diamonds (MR winds) and purple and green triangles (OH and OI FPI winds, respectively).

meridional components in both the MR and FPI winds. Although the FPI winds at two emission layers show consistent local time variations and tidal structures with the MR winds, the amplitudes of the local time variations of the FPI winds are smaller than the MR winds. As depicted in Figure 6, this feature may also show that the FPI observation tends to be smaller than the wind compared to the MR observation. Entire nighttime wind profiles from the MR for 60 days around the June solstice are presented in the right panels of Figure 7. The strength of wind variability keeps increasing with the height but the variabilities of the FPI winds appear to be smaller than the MR winds, which implies that the FPI tends to smooth out high speed winds probably due to spatial variations of the emission layers.

4. Summary and Conclusion

We have compared the nocturnal MLT wind measurements simultaneously performed by the FPI and MR at KSS for winter season in 2017 and 2019. Instead of assuming stationary heights for airglow emission layers, the temporal variations of the airglow emission heights were derived from the daily meteor peak height (MPH) and the height width of the meteor distribution obtained from the MR observations to apply to the wind comparison between two observations. The OH volume mixing ratio derived from Aura/MLS shows that the OH molecules mostly exist at a fixed pressure surface. Emission peak heights, estimated from the vertical structure of volume emission rate for two OH emissions from TIMED/SABER, are found to slightly increase from the evening to morning especially at the OH-1.6 μm emission layer. The MPH shows similar local time variations, reflecting background atmospheric pressure surfaces. The height integrated emission rate is inversely correlated with the emission peak height and slightly decreases with local time at night. The OH emission intensity from the FPI also similarly varies with local time.

We calculated weighted mean MR winds at 11 height bins within 12 km FWHM using Gaussian curves to approximate the two emission layer winds measured by the FPI. Two airglow emission heights derived from the correlation analysis of FPI-MR wind measurements well agree with generally accepted emission altitudes of 87 and 97 km for OH and OI, respectively.

Instantaneous wind comparison of two observations notably shows that greater variability at the height of the OI airglow layer due to small-scale gravity waves propagating to higher altitude.

In the comparison with the MR winds, the FPI winds show most of the characteristics of the neutral winds at two emission layers such as local time variations and semidiurnal tide structures. However, we found that FPI wind tends to be smaller compared to the MR wind and the discrepancy of the FPI wind with that of MR becomes stronger at OI emission layer at which larger wind perturbations exist.

It was found that the correlation coefficient and the slope of the FPI-MR winds are closely associated with sky temperature and a careful selection of the sky temperature threshold is needed to minimize the unintended discrepancies between two wind measurement techniques. Although the FPI winds under clear night better agree with the MR winds, they are still smaller than the MR winds. This difference presents that the spatiotemporal characteristics of the airglow emission layers should be considered when wind data from different measurements are combined.

Data Availability Statement

The TIMED/SABER data are available from http://saber.gats-inc.com/. The OH volume mixing ratio and geopotential height data from the Aura MLS team are also gratefully acknowledged. The Aura/MLS data can be accessed at http://disc.sci.gsfc.nasa.gov/Aura/data-holdings/MLS. The KSS FPI and meteor radar data are provided by Korea Polar Research Institute through the Korea Polar Data Center (https://kpdc.kopri.re.kr).

Acknowledgments
This study was supported by the grant PE21020 from Korea Polar Research Institute. QW is supported by NCAR, which is funded by the National Science Foundation. The authors would like to thank the TIMED SABER team for providing the OH volume emission rate (version 2.0) data.

References

Baker, D. J., & Stair, A. T. (1988). Rocket measurements of the altitude distributions of the hydroxyl airglow. *Physica Scripta*, *37*(4), 611–622. https://doi.org/10.1088/0031-8949/37/4/021

Baker, D. J., Thurgood, B. K., Harrison, W. K., Mlynczak, M. G., & Russell, J. M. (2007). Equatorial enhancement of the nighttime OH mesospheric infrared airglow. *Physica Scripta*, *75*(5), 615–619. https://doi.org/10.1088/0031-8949/75/5/004

Baumgaertner, A. J. G., & McDonald, A. J. (2007). A gravity wave climatology for Antarctica compiled from Challenging Minisatellite Payload/Global Positioning System (CHAMP/GPS) radio occultations. *Journal of Geophysical Research*, *112*, D05103. https://doi.org/10.1029/2006JD007504

Dunker, T. (2018). The airglow layer emission altitude cannot be determined unambiguously from temperature comparison with lidars. *Atmospheric Chemistry and Physics*, *18*(9), 6691–6697. https://doi.org/10.5194/acp-18-6691-2018

Espy, P. J., Jones, G. O. L., Swenson, G. R., Tang, J., & Taylor, M. J. (2004). Seasonal variations of the gravity wave momentum flux in the Antarctic mesosphere and lower thermosphere. *Journal of Geophysical Research*, *109*, D23109. https://doi.org/10.1029/2003JD004446

Fritts, D. C., Iimura, H., Lieberman, R., Janches, D., & Singer, W. (2012). A conjugate study of mean winds and planetary waves employing enhanced meteor radars at Rio Grande, Argentina (53.8°S) and Juliusruh, Germany (54.6°N). *Journal of Geophysical Research*, *117*, D05117. https://doi.org/10.1029/2011JD016305

Gao, H., Xu, J., & Wu, Q. (2010). Seasonal and QBO variations in the OH nightglow emission observed by TIMED/SABER. *Journal of Geophysical Research*, *115*, A06313. n/a. https://doi.org/10.1029/2009JA014641

Ghosh, S. N. (2002). The Neutral Upper Atmosphere. *The Neutral Upper Atmosphere*, *249*. https://doi.org/10.1007/978-94-017-0071-9

Greet, P. A., Murphy, D. J., Vincent, R., & Dyson, P. L. (2000). A comparison of optical and radar measurements of mesospheric winds and tides. *Geophysical Research Letters*, *27*(16), 2477–2480. https://doi.org/10.1029/2000gl000036

Harding, B. J., Ridley, A. J., & Makela, J. J. (2019). Thermospheric Weather as Observed by Ground-Based FPIs and Modeled by GITM. *Journal of Geophysical Research: Space Physics*, *124*, 1307–1316. https://doi.org/10.1029/2018JA026032

Jee, G., Kim, J.-H., Lee, C., & Kim, Y. H. (2014). Ground-based Observations for the Upper Atmosphere at King Sejong Station, Antarctica. *Journal of Astronomy and Space Sciences*, *31*(2), 169–176. https://doi.org/10.5140/JASS.2014.31.2.169

Kam, H., Jee, G., Kim, Y., Ham, Y.-B., & Song, I.-S. (2017). Statistical analysis of mesospheric gravity waves over King Sejong Station, Antarctica (62.2°S, 58.8°W). *Journal of Atmospheric and Solar-Terrestrial Physics*, *155*, 86–94. https://doi.org/10.1016/j.jastp.2017.02.006

Kwon, H.-J., Lee, C., Jee, G., Ham, Y.-b., Kim, J.-H., Kim, Y. H., et al. (2018). Ground-based Observations of the Polar Region Space Environment at the Jang Bogo Station, Antarctica. *Journal of Astronomy and Space Sciences*, *35*(3), 185–193. https://doi.org/10.5140/JASS.2018.35.3.185

Larsen, M. F. (2002). Winds and shears in the mesosphere and lower thermosphere: Results from four decades of chemical release wind measurements. *Journal of Geophysical Research*, *107*(A8), 28. SIA 28–1–SIA 28–14. https://doi.org/10.1029/2001JA000218

Lee, C., Jee, G., Kim, J.-H., & Song, I.-S. (2018a). Meteor echo height ceiling effect and mesospheric temperature estimation from meteor radar observations. *Annales Geophysicae*, *36*(5), 1267–1274. https://doi.org/10.5194/angeo-36-1267-2018

Lee, C. S., Younger, J. P., Reid, I. M., Kim, Y. H., & Kim, J.-H. (2013). The effect of recombination and attachment on meteor radar diffusion coefficient profiles. *Journal of Geophysical Research: Atmospheres*, *118*, 3037–3043. https://doi.org/10.1002/jgrd.50315

Lee, W., Kim, Y. H., Lee, C., & Wu, Q. (2018b). First Comparison of Mesospheric Winds Measured with a Fabry-Perot Interferometer and Meteor Radar at the King Sejong Station (62.2°S, 58.8°W). *Journal of Astronomy and Space Sciences*, *35*(4), 235–242. https://doi.org/10.5140/JASS.2018.35.4.235

Liu, G., & Shepherd, G. G. (2006). An empirical model for the altitude of the OH nightglow emission. *Geophysical Research Letters*, *33*, L09805. https://doi.org/10.1029/2005GL025297

Liu, G., Shepherd, G. G., & Roble, R. G. (2008). Seasonal variations of the nighttime O(1S) and OH airglow emission rates at mid-to-high latitudes in the context of the large-scale circulation, *Journal of Geophysical Research*, *113*, A06302. https://doi.org/10.1029/2007JA012854

Matsuda, T. S., Nakamura, T., Ejiri, M. K., Tsutsumi, M., & Shiokawa, K. (2014). New statistical analysis of the horizontal phase velocity distribution of gravity waves observed by airglow imaging. *Journal of Geophysical Research: Atmospheres*, *119*, 9707–9718. https://doi.org/10.1002/2014JD021543

Meriwether, J. W. (2006). Studies of thermospheric dynamics with a Fabry-Perot interferometer network: A review. *Journal of Atmospheric and Solar-Terrestrial Physics*, *68*(1), 1576–1589. https://doi.org/10.1016/j.jastp.2005.11.014

Park, J., Lühr, H., Lee, C., Kim, Y. H., Jee, G., & Kim, J.-H. (2014). A climatology of medium-scale gravity wave activity in the midlatitude/low-latitude daytime upper thermosphere as observed by CHAMP. *Journal of Geophysical Research: Space Physics*, *119*, 2187–2196. https://doi.org/10.1002/2013JA019705

Phillips, A., Manson, A. H., Meek, C. E., & Llewellyn, E. J. (1994). A long-term comparison of middle atmosphere winds measured at Saskatoon (52°N, 107°W) by a medium-frequency radar and a Fabry-Perot interferometer. *Journal of Geophysical Research*, *99*(D), 12923. https://doi.org/10.1029/94JD00618

Pickett, H. M., Read, W. G., Lee, K. K., & Yung, Y. L. (2006). Observation of night OH in the mesosphere. *Geophysical Research Letters*, *33*, L19808. https://doi.org/10.1029/2006GL026910

Plagmann, M., Marsh, S. H., Baggaley, W. J., Bennett, R. G. T., Deutsch, K. A., Fraser, G. J., et al. (1998). Annual variation of airglow heights derived from wind measurements. *Geophysical Research Letters*, *25*(24), 4457–4460. https://doi.org/10.1029/1998GL900212

Reid, I. M., Spargo, A. J., Woithe, J. M., Klekociuk, A. R., Younger, J. P., & Sivjee, G. G. (2017). Seasonal MLT-region nightglow intensities, temperatures, and emission heights at a Southern Hemisphere midlatitude site. *Annales Geophysicae*, *35*(3), 567–582. https://doi.org/10.5194/angeo-35-567-2017

Sandford, D. J., Beldon, C. L., Hibbins, R. E., & Mitchell, N. J. (2010). Dynamics of the Antarctic and Arctic mesosphere and lower thermosphere - Part 1: Mean winds. *Atmospheric Chemistry and Physics*, *10*(2), 10273–10289. https://doi.org/10.5194/acp-10-10273-2010

Savigny, von, C., McDade, I. C., Eichmann, K. U., & Burrows, J. P. (2012). On the dependence of the OH *Meinel emission altitude on vibrational level: SCIAMACHY observations and model simulations. *Atmospheric Chemistry and Physics*, *12*(18), 8813–8828. https://doi.org/10.5194/acp-12-8813-2012

Schwartz, M. J., Lambert, A., Manney, G. L., Read, W. G., Livesey, N. J., Froidevaux, L., et al. (2008). Validation of the aura microwave limb sounder temperature and geopotential height measurements. *Journal of Geophysical Research - D: Atmospheres*, *113*, D15S11. https://doi.org/10.1029/2007JD008783

Sheese, P. E., Llewellyn, E. J., Gattinger, R. L., & Strong, K. (2014). OH Meinel band nightglow profiles from OSIRIS observations. *Journal of Geophysical Research: Atmospheres*, *119*(19), 11417–11428. https://doi.org/10.1002/2014jd021617

Smith, A. K., Marsh, D. R., Mlynczak, M. G., & Mast, J. C. (2010). Temporal variations of atomic oxygen in the upper mesosphere from SABER. *Journal of Geophysical Research*, *115*, D18309. https://doi.org/10.1029/2009JD013434

Taylor, M. J., Bishop, M. B., & Taylor, V. (1995). All-sky measurements of short period waves imaged in the OI(557.7 nm), Na(589.2 nm) and near infrared OH and O2(0,1) nightglow emissions during the ALOHA-93 Campaign. *Geophysical Research Letters*, *22*(20), 2833–2836. https://doi.org/10.1029/95GL02946

Won, Y.-I., Cho, Y.-M., Lee, B. Y., & Kim, J. (2001b). Studies of Gravity Waves Using Michelson Interferometer Measurements of OH (3-1) Bands. *Journal of Astronomy and Space Sciences*, *18*(1), 21–26.

Won, Y.-I., Cho, Y.-M., Niciejewski, R. J., & Kim, J. (2001a). Observations of OH(3,1) airglow emission using a Michelson interferometer at 62° S. *Advances in Space Research*, *27*(6/7), 1165–1170. https://doi.org/10.1016/S0273-1177(01)00192-2

Won, Y.-I., Niciejewski, R. J., Killeen, T. L., Johnson, R. M., & Lee, B. Y. (1999). Observations of high-latitude lower thermospheric winds from Thule Air Base and Søndre Strømfjord, Greenland. *Journal of Geophysical Research*, *104*(A1), 25–32. https://doi.org/10.1029/1998JA900059

Wu, Q., Gablehouse, R. D., Solomon, S. C., Killeen, T. L., & She, C.-Y. (2004). In C. A. Nardell, P. G. Lucey, J.-H. Yee, & J. B. Garvin (Eds.), *A new Fabry-Perot interferometer for upper atmosphere research* (Vol. 5660, pp. 218–227). SPIE. Retrieved from https://www.spiedigitallibrary.org/conference-proceedings-of-spie/5660/0000/A-new-Fabry-Perot-interferometer-for-upper-atmosphere-research/10.1117/12.573084.short

Wu, Q., McEwen, D., Guo, W., Niciejewski, R. J., Roble, R. G., & Won, Y.-I. (2008). Long-term thermospheric neutral wind observations over the northern polar cap. *Journal of Atmospheric and Solar-Terrestrial Physics*, *70*(16), 2014–2030. https://doi.org/10.1016/j.jastp.2008.09.004

Wüst, S., Schmidt, C., Hannawald, P., Bittner, M., Mlynczak, M. G., & Russell, J. M. III. (2019). Observations of OH airglow from ground, aircraft, and satellite: Investigation of wave-like structures before a minor stratospheric warming. *Atmospheric Chemistry and Physics*, *19*(9), 6401–6418. https://doi.org/10.5194/acp-19-6401-2019

Xu, J., Smith, A. K., Jiang, G., Gao, H., Wei, Y., Mlynczak, M. G., & Russell, J. M. III. (2010). Strong longitudinal variations in the OH nightglow, *Geophysical Research Letters*, *37*, L21801. https://doi.org/10.1029/2010GL043972

Yee, J. H., & Abreu, V. J. (1987). Mesospheric 5577Å green line and atmospheric motions-Atmosphere explorer satellite observations. *Planetary and Space Science*, *35*(11), 1389–1395. https://doi.org/10.1016/0032-0633(87)90051-1

Yee, J.-H., Crowley, G., Roble, R. G., Skinner, W. R., Burrage, M. D., & Hays, P. B. (1997). Global simulations and observations of O(1S), O2(1Σ) and OH mesospheric nightglow emissions. *Journal of Geophysical Research*, *102*(A9), 19949–19968. https://doi.org/10.1029/96JA01833

Yu, T., Xia, C., Zuo, X., Huang, C., Mao, T., Liu, L., & Liu, Z. (2016). A comparison of mesospheric and low-thermospheric winds measured by Fabry-Perot interferometer and meteor radar over central China. *Journal of Geophysical Research: Space Physics*, *121*, 10037–10051. https://doi.org/10.1002/2016JA022997

Yu, T., Zuo, X., Xia, C., Li, M., Huang, C., Mao, T., et al. (2017). Peak height of OH airglow derived from simultaneous observations a Fabry-Perot interferometer and a meteor radar. *Journal of Geophysical Research: Space Physics*, *122*, 4628–4637. https://doi.org/10.1002/2016JA023743

Zhang, S. P., & Shepherd, G. G. (1999). The influence of the diurnal tide on the O(^{1}S) and OH emission rates observed by WINDII on UARS. *Geophysical Research Letters*, *26*(4), 529–532. https://doi.org/10.1029/1999GL900033